Nanocomposite Catalysts Producing Durable, Super-Black Carbon Nanotube Systems: Applications in Solar Thermal Harvesting

Nikolaos T. Panagiotopoulos,[†,‡] Evmorfia K. Diamanti,[†] Loukas E. Koutsokeras,[§] Maria Baikousi,[†] Evangelos Kordatos,[†] Theodore E. Matikas,[†] Dimitrios Gournis,[†] and Panos Patsalas[†,§,*]

[†]Department of Materials Science and Engineering and [‡]Department of Physics, University of Ioannina, GR-45110 Ioannina, Greece and [§]Research Unit for Nanostructured Materials Systems, Department of Mechanical Engineering and Materials Science and Engineering, Cyprus University of Technology, P.O. Box 50329, Limassol 3603, Cyprus

ABSTRACT A novel two-step approach for preparing carbon nanotube (CNT) systems, exhibiting an extraordinary combination of functional properties, is presented. It is based upon nanocomposite films consisting of metal (Me = Ni, Fe, Mo, Sn) nanoparticles embedded into diamond-like carbon (DLC). The main concept behind this approach is that DLC inhibits the growth of Me, resulting in the formation of small nanospheres instead of layers or extended grains. In the second step, DLC:Me substrates were used as catalyst templates for the growth of CNTs by the thermal chemical vapor deposition (T-CVD) process. X-ray photoelectron spectroscopy (XPS) has shown that at the T-CVD temperature of 700 °C DLC is completely graphitized and NiC is formed, making DLC:Ni a very effective catalyst for CNT growth. The catalyst layers and the CNT systems have been characterized with a wide range of analytical techniques such as Auger electron spectroscopy and X-ray photoelectron spectroscopy (AES/XPS), X-ray diffraction, reflectivity and scattering, Raman spectroscopy, scanning electron microscopy, atomic force microscopy, and optical and electrical testing. The produced CNTs are of excellent quality, without needing any further purification, durable, firmly attached to the substrate, and of varying morphology depending on the density of catalyst nanoparticles. The produced CNTs exhibit exceptional properties, such as super-hydrophobic surfaces (contact angle up to 165°) and exceptionally low optical reflection (reflectivity $<10^{-4}$) in the entirety of the visible range. The combination of the functional properties makes these CNT systems promising candidates for solar thermal harvesting, as it is demonstrated by solar simulation experiments.

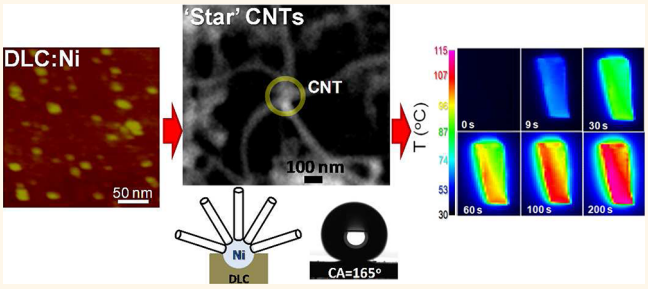

KEYWORDS: carbon nanotubes · light absorbers · nanocomposites · pulsed laser deposition · chemical vapor deposition · XPS

Since their discovery, carbon nanotubes (CNTs) have evolved into one of the most dynamic paradigms of modern materials science. Today their production and applications are among the more mature engineering fields; in particular, the emerging applications of CNTs include super-black light absorbers,[1] solar harvesting,[2,3] photonic devices,[4,5] and thermal management systems.[6,7] One of the most effective production processes for CNTs is chemical vapor deposition (CVD);[8−19] the structural quality and morphology of CVD-produced CNTs are affected by the carbon precursor (methane, ethylene, acetylene, xylene, or ethanol),[8] the gas mixture flow,[9] and the level of impurities.[10] However, the most essential issue for the CVD growth of CNTs is the required catalyst,[11−19] with Ni,[11,14,15] Fe,[11,14−17] Co,[11,14,15] and their bimetallic alloys[11−13,16] being the most widely used cases, due to their low miscibility with C and their activity in forming graphitic rings.[11] In addition to the physicochemical properties of these catalysts, their morphology has been proven to be very important, as well; therefore, great research efforts have been carried out to design and optimize nanocatalysts for specific CNT architectures and applications.[15−19]

* Address correspondence to ppats@cc.uoi.gr.

Received for review March 10, 2012 and accepted November 5, 2012.

Published online November 05, 2012
10.1021/nn304531k

In particular, nanoparticles (NPs) or thin films of Ni have been considered as effective catalysts for CNT growth,[12,14,15] and recently, the mechanism of graphitization of carbon near nanostructured Ni surfaces has been explained.[20] Therefore, the morphological control of metal particles at the nanoscale can be an effective way of controlling the morphology and the functional properties of CNT arrays.

Pulsed laser deposition (PLD) has been previously used for the growth of nanocomposite films consisting of metal nanospheres embedded into a dielectric matrix, such as diamond-like carbon (DLC)[21] or AlN;[22] the main concept behind this approach is that during the successive carbon−metal deposition the DLC inhibits the growth of the metal, resulting in the formation of small (∼10 nm) metal nanospheres instead of metal layers or extended grains.[21] We show here that such an approach is very promising for the production of nanocomposite, metal-containing, catalytic surfaces for the thermal CVD (T-CVD) growth of CNTs.

In this work, we demonstrate that a novel, simple, two-step process, based on metal-containing DLC (DLC:Me, Me = Ni, Fe, Mo, Sn) nanocomposite catalyst layers can grow CNTs of varying morphology (from aligned to interlinked, "star"-shaped CNTs) and exceptional functional properties (superhydrophobic surfaces with contact angle up to 165°, and extremely low, $<10^{-4}$, optical reflectance) without further purification or post-growth processing; composite films of SiC and AlN matrices have also been implemented for comparison purposes. Finally, we demonstrate that the combination of the functional properties makes these CNT systems promising candidates for solar thermal harvesting, by exposing the produced CNT systems to concentrated solar light of realistic power and monitoring their photothermal behavior for the first time; our demonstration implies that CNT systems may find new applications in photothermal technology.

RESULTS AND DISCUSSION

Growth and Characteristics of DLC:Me Catalysts. First, a composite catalyst layer is grown on Si substrates by pulsed laser deposition (PLD) using a sectored target consisting of the matrix material (DLC, SiC, or AlN) and metal (Ni, Fe, Mo, or Sn) sectors of varying area (see Supporting Information). This process results in nanocomposite films consisting of metal nanospheres embedded into the matrix material. In particular, for the Ni particles, their size lies in the range of approximately 10−30 nm; the Ni particles appear as bright protrusions in the atomic force microscopy (AFM) image of Figure 1a, which corresponds to sample A. Then, the DLC:Me/Si specimens are used as growth templates for T-CVD of CNTs at 700 °C using acetylene as the carbon source. T-CVD of CNTs has also been implemented on SiC:Ni, AlN:Ni, and pure Ni catalyst layers grown by PLD and sputtering for comparison. The growth parameters

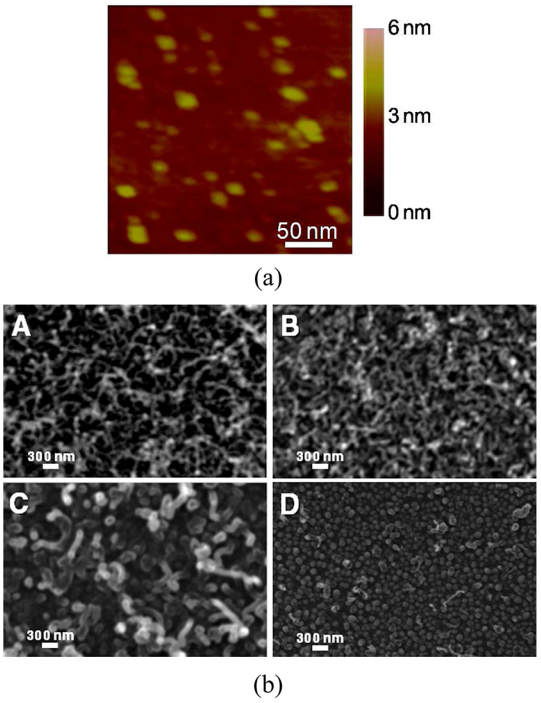

Figure 1. (a) AFM image from a DLC:Ni template (sample A) before the growth of CNTs, (b) SEM images of CNTs grown by various conditions on DLC:Ni (the capital letters correspond to the data of Table 1).

used for the various nanocomposite catalysts of this study are summarized in Table 1.

An essential issue is the accurate description of the chemistry of the outer surface of the catalyst layer, which is exactly the part of the catalyst that reacts with the flowing acetylene to form CNTs during T-CVD; Auger electron spectroscopy (AES) fulfils the criterion of being surface-sensitive,[21,23] and thus, it has been employed for the determination of the Me content in all samples and the fraction of the sp^3-bonded carbon on the surface of DLC:Me samples. In the case of Ni nanoparticles, the particle sizes on the DLC:Ni surface have been determined from AFM images. The Me content in DLC:Me has been determined from the relative strength of the C_{KVV} and metal (Ni_{LMM}, Fe_{LMM}, Sn_{MNN}, Mo_{MNN}) peaks manifested in the *in situ* AES differential spectra, taking into account the corresponding sensitivity factors (see Table 1 and the Supporting Information). Note that the small Me atomic concentration corresponds to higher geometric surface coverage (SC) of metal, as shown in the AFM image of Figure 1a (sample A) because of the different ionic radii of metals and C. The C hybridization (sp^3/sp^2 ratio) has been determined from the broadening of the C_{KVV} peak[21,23] and has been confirmed by analyzing the C 1s envelope of X-ray photoelectron spectra (XPS)[23−25] for selected samples. The thickness, the density, and the surface roughness of the nanocomposite catalyst layers have been determined by X-ray reflectivity (XRR) following the analysis presented in ref 25. The main structural

TABLE 1. Growth Parameters and Structural/Chemical Features of the Nanocomposite Catalyst Thin Film Templates

sample	technique	matrix material	metal	metal on surface (atom %)	density (g/cm^3)	thickness (nm)	surface roughness (nm)
A	PLD	DLC	Ni	5.0	2.5 ± 0.2	35	1
B		DLC	Ni	6.0	2.7 ± 0.2	23	2
C		DLC	Ni	7.0	3.1 ± 0.2	26	10
D		DLC	Ni	11.0	3.3 ± 0.2	26	6
E		DLC	Mo	2.5	2.9 ± 0.2	28	1
F		DLC	Sn	4.5	2.5 ± 0.2	59	2
G		DLC	Fe	1.0	2.0 ± 0.2	31	1
H		SiC	Ni	3.5	3.4 ± 0.2	30	1
I		AlN	Ni	4.0	3.2 ± 0.2	28	1
J			Ni	100.0			
K	sputtering		Ni	100.0			

and chemical features of the nanocomposite catalysts are summarized in Table 1.

Structural and Morphological Features of CNTs and the Effect of Catalyst Composition. The CNT layers, which have been grown on the DLC:Ni templates, are purely graphitic, according to XPS and AES analysis (see Supporting Information), and exhibit strong morphological variations that are dictated predominantly by the [Ni] concentration on the DLC:Ni surface. This is revealed by the plan-view SEM images presented in Figure 1b; the capital letters of the SEM images correspond to the relevant samples in Table 1.

Samples A and B exhibit strongly interlinked CNT bundles of star shape (for a detailed image, refer to Figure 4e, as well), resembling the octopus-type CNT growth.[26,27] Although configurations of several CNTs starting from a single Ni particle have been observed to follow both base[26] and tip[26,27] growth mode, in our case, the CNTs follow strictly the base growth when DLC:Ni catalysts are used, as it has been revealed by the XPS wide-scan spectra of Figure 2a. Indeed, the surface of sample B consists predominantly of C and Ni and some O attributed to environmental adsorbates, such as OH groups due to humidity in the laboratory environment. After *in situ* annealing in the analysis chamber at 700 °C (*i.e.*, the temperature of T-CVD of CNTs), the O contamination has been significantly reduced; after the growth of CNTs, no traces of Ni exist and the surface consists exclusively of C, indicating a pure base growth of CNTs. Our findings regarding the base growth of CNTs oppose the results of El Mel *et al.*,[28] who used hydrogenated DLC:Ni catalyst templates and observed a clear tip growth of CNTs; however, this difference is quite well understood. The PLD-grown, unhydrogenated DLC matrix is harder[29] and more dense[23,30] compared to the hydrogenated amorphous carbon used by El Mel *et al.*[28] Hence, it is expected that the Ni diffusion will be less pronounced and the Ni nanoparticles are attached more firmly in the unhydrogenated DLC matrix in our case, compared to the soft and underdense, hydrogenated carbon. Similar XPS experiments have been carried out for all DLC:Me catalysts used in this study. CNTs grown using nanocomposite catalysts that incorporate Ni or Fe follow the base growth since no metal has been detected on the surface after T-CVD, while the use of DLC:Mo catalysts results in a tip growth of CNTs (XPS did detect Mo on the surface; refer to Supporting Information for more details). Finally, the DLC:Sn is a very unstable catalyst due to the low melting point of Sn, which results in outdiffusion of Sn at 700 °C (*i.e.*, the T-CVD growth of CNTs) and agglomeration into micrometer metal droplets that serve as selective nucleation sites of CNTs on the DLC surface.

XPS was used for the identification of the CNT growth mechanism from the DLC:Ni catalyst by detailed analysis of the Ni 2p and C 1s high-resolution spectra shown in Figure 2b–e. In particular, the Ni 2p doublet of the as-deposited sample B exhibits a fine structure with contributions attributed to metallic Ni (853.2 eV for the Ni $2p_{3/2}$) and NiO_2 or $Ni(OH)_2$ (856.3 eV for the Ni $2p_{3/2}$);[31,32] after *in situ* annealing, the peak at 856.3 eV disappeared, confirming that it originates from $Ni(OH)_2$. The hydroxyl groups desorbed after annealing, and a clean Ni surface remained around the particle. Further insights can be extracted from the analysis of the C 1s peak (Figure 2c–e); the C 1s peak has been analyzed to contributions of contamination carbon (blue lines), C–C sp^2 bonds (red), C–C sp^3 bonds (magenta), and Ni–C bonds (green). The contamination carbon itself consists of several types of bonds (*e.g.*, C–O, C–OH, *etc.*); in order to minimize the fitting parameters, the C 1s peak has been measured for a variety of non-carbonaceous samples (Si wafers, Ag, Au, and Cu films) exposed intentionally to lab atmosphere, in order to identify the contribution of contamination carbon and then to use it as a fixed line shape in the fitting procedure. The as-deposited sample exhibited predominantly sp^2 C–C bonds and a minority of sp^3 C–C bonds, characteristic of amorphous carbon.[33,34] The peak assigned to the C–C sp^2 bonds exhibits a full width at half-maximum (fwhm) of 1.6 eV that lies in the range of 1.4–1.8 eV, which is characteristic of amorphous carbon.[23,33,34] During *in situ* annealing, the contributions of C–C sp^3 bonds are eliminated, indicating a complete graphitization,

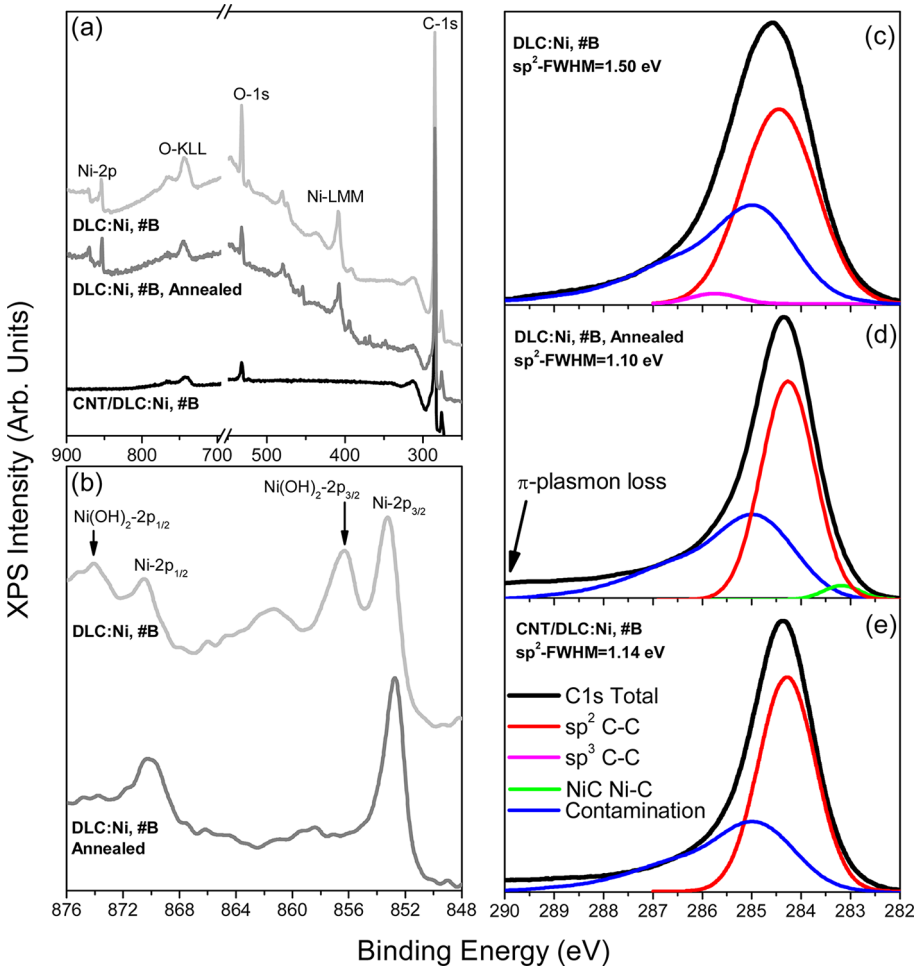

Figure 2. XPS spectra of sample B: (a) wide scan spectra of as deposited sample (light gray), during *in situ* annealing at the temperature of T-CVD growth of CNTs (dark gray) and after CNT growth (black); (b) Ni 2p spectra of as-deposited sample (light gray) and during *in situ* annealing (dark gray); (c) C 1s spectrum of as-deposited sample; (d) C 1s spectrum during *in situ* annealing; (e) C 1s spectrum after CNT growth; the C 1s spectra have been deconvoluted into contributions of contamination carbon (blue), C−C sp^2 bonds (red), C−C sp^3 bonds (magenta), and Ni−C bonds (green).

and the broadening of the peak of the C−C sp^2 bonds is substantially reduced, below the range of amorphous carbon, which is a clear indication of reduction of disorder of sp^2-bonded carbon and of the formation of graphene layers. In addition, a weak peak (283.2 eV) characteristic of Ni−C bonds[35,36] emerged during annealing. Nickel carbide is a good precursor for the formation of graphene layers because of its low lattice mismatch to the Ni(111) planes, as well as due to energetic reasons;[37,38] hence, a Ni(111)-faceted nanoparticle can effectively fold the graphene planes and can act as a nucleation site for CNT growth. Our observations are also in accordance with previous experimental[39,40] and computational[41,42] works identifying metal carbides as effective precursors of CNT growth. It is noteworthy, however, that in our case the formation of the Ni−C bonds and the subsequent development of the initial graphene layers start even without the flow of the hydrocarbon precursor, due to the existence of the DLC matrix in the nanocomposite catalyst. Therefore, the development of the CNTs does not rely exclusively on the feed and diffusion of the volatile hydrocarbon; instead, the nucleation of CNTs starts from the carbonaceous catalyst itself.

The main difference between the CNTs of samples A and B is their average density; in particular, sample A is not fully covered, and bundles of interlinked CNTs with an average diameter of about 40 nm coexist with dark (empty) regions in the corresponding SEM image. The SEM image of sample B reveals a similar geometry of interlinked CNTs, which, however, fully cover the DLC:Ni catalyst. The diameters of CNTs of samples A and B are consistent with the Ni particle size for star or octopus geometry according to the analysis of Saavedra *et al.*[27] On the contrary, for higher Ni content in the catalyst (sample C), the CNTs become thicker (>100 nm); in that case, the interlinking of CNTs is substantially reduced. Finally, sample D, which is the one with the maximum Ni content in the corresponding DLC:Ni catalyst template, is characterized by highly aligned, thick (>100 nm) multiwalled CNTs.

The integrity and durability of all of the CNT systems grown using the DLC:Ni catalyst templates are substantial.

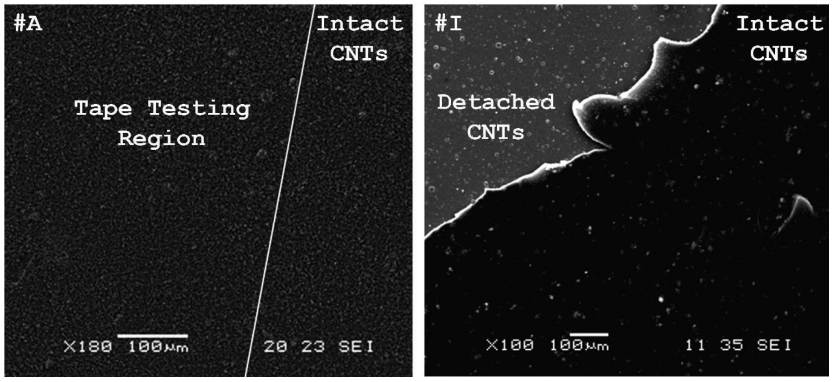

Figure 3. SEM images from samples A (left) and I (right) after tape testing.

Unlike the CNTs grown on pure Ni, either sputtered, PLD-grown, or on Ni foils,[43] the CNT samples grown on the DLC:Ni templates endured duct tape testing, blowing with >3 bar compressed air and ultrasonication in water (for 5 min), as shown for sample A in the left-hand SEM images of Figure 3; indeed, there is no apparent distinction between the left side, which was forced to duct tape testing, and the as-grown right part of the sample (the white line defines the border of intact and tape-tested regions). The integrity of the sample is only challenged by ultrasonication in methanol (refer also to Supporting Information). On the contrary, the CNTs grown on the AlN:Ni nanocomposite catalyst layer (sample I) are easily peeled off and detached, as it is demonstrated in the right SEM image of Figure 3. This striking difference of the adhesion of the CNTs, for different matrix material of the composite catalyst, is explained by the mechanism of CNT growth on DLC:Ni that we have explained previously. In particular, when the dense and rigid DLC:Ni catalysts are used, the nucleation starts from the catalyst layer itself, resulting in better adhesion compared to the samples grown on pure metal or on nanocomposites with a non-carbonaceous matrix.

The surface morphology of CNTs cannot be studied by XRR because their surfaces are too rough, or by AFM, due to the flexibility of the CNT tips that are swinging when an AFM tip is approaching. Therefore, the qualitative results deduced previously from the SEM observations have been confirmed and quantified by off specular X-ray reflectivity analysis, which is appropriate for the study of rough surfaces.[44,45] The CNTs' density has been determined from the critical angle,[25] which according to the distorted-wave Born approximation (DWBA) is manifested as the low-angle Yoneda wing in the off specular reflectivity scan (refer to Supporting Information).[44] The evolution of density of the CNT samples *versus* the metal content on the nanocomposite catalysts is presented in Figure 4a. The evolution of density is similar for the CNTs grown on DLC:Ni (black diamonds) and DLC:Fe (red triangle) due to a similar growth mechanism. It is evident that sample D ([Ni] = 11 atom %) is almost as dense as graphite, proving that the aligned CNTs are densely packed. As the CNTs become less aligned, the average density is indeed reduced, confirming the SEM observations; finally, samples A and G, which exhibit the less packed morphology in the SEM images, are substantially underdense. On the contrary, the samples H (CNTs/SiC:Ni) and I (CNTs/AlN:Ni) are denser compared to the equivalent samples grown on DLC:Ni and DLC:Fe, due to the their inferior structural quality, as evidenced by Raman spectroscopy (Figure 4b), which will be discussed in detail below. The densities of samples E (CNTs/DLC:Mo) and F (CNTs/DLC:Sn) are further increased due to the tip growth of CNTs on DLC:Mo, as shown by the SEM image of Figure 4c, revealing needle-like CNTs terminating in bright particles, which are Mo according to XPS analysis (refer to Supporting Information for more details), and the outdiffusion and agglomeration of Sn during T-CVD; in both DLC:Mo and DLC:Sn cases, the result is the enrichment of surfaces of samples E and F by metal, which is denser than carbon.

An estimate of the surface roughness can be deduced from the ratio of intensities of the satellite Yoneda wings and the specular peak, $I_{Yoneda}/I_{specular}$ ratio, in the X-ray data[44,45] (refer to Supporting Information), as shown in Figure 4d. Sample A, which is not fully covered and its CNTs are growing in star-shape geometries (Figure 4e,f), is the rougher one. The surface roughness (that is associated with the $I_{Yoneda}/I_{specular}$ ratio) is gradually reduced as the sample is fully covered by CNTs (sample B) and the CNTs become gradually more aligned and close-packed (samples C and D, Figure 4g). The variation of the surface roughness of the CNTs has a severe effect on their hydrophobicity. Thus, the interlinked and most rough sample A is super-hydrophobic (water contact angle 165°, exceeding the super-hydrophobic limit of 150°, due to the two scales of surface features, *i.e.*, ~30 nm tube diameter and ~1 μm CNT bundle width), while the most aligned and smooth sample D exhibits an intermediate water contact angle (93°). Another confirmation of the morphology of the grown CNTs over the DLC:Ni catalysts has also been provided

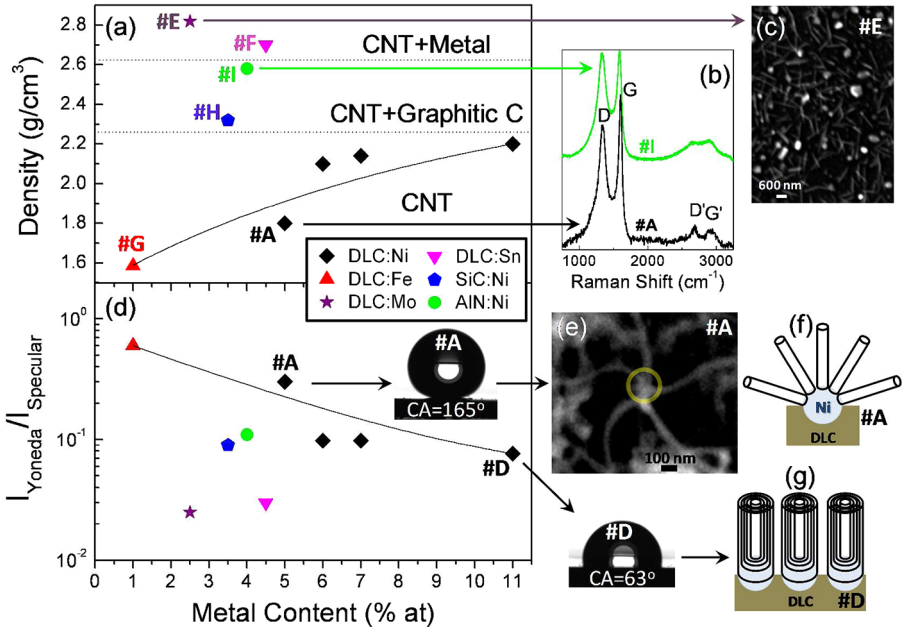

Figure 4. (a) Variation of the CNT layer density, (b) Raman spectra from CNTs grown using DLC:Ni and AlN:Ni catalysts, (c) SEM image of CNTs grown using DLC:Mo catalyst, (d) ratio of the intensity of the Yoneda wings over the specular X-ray reflectivity, which is associated with the surface roughness (the insets depict the water contact angles for samples A and D), (e) high-resolution SEM image demonstrating the star-shape geometry of CNTs in sample A, (f,g) sketches displaying the correlation between the Ni nanoparticle density and the CNT's morphology for samples A and D.

by four-probe electrical measurements. According to the analysis of the *I*−*V* measurements, all of the CNT systems were conducting with electrical resistance values ranging between 1.7 and 110 kΩ, which are typical for CNTs of similar length[46] due to the morphology variations.

In addition to the study of the morphological features, Raman spectroscopy was used to evaluate the structural quality of the produced CNTs. The Raman spectra of all of the produced CNTs/DLC:Ni samples exhibit the main characteristic graphitic Raman features[13,47,48] at around 1340 and 1600 cm^{-1} corresponding to graphite D (disordered) and G (tangential stretching E_{2g} mode) bands, respectively,[29,30] and the corresponding second-order D′ and G′ bands at 2690 and 2900 cm^{-1}, respectively. The relative intensity of D and G bands (I_D/I_G) reveals the degree of disorder in the graphitic sheets;[13,47] it was found that that more ordered CNT samples correspond to lower I_D/I_G ratios and sharper G peaks.[48] The Raman results indicate that the structural features of the grown CNTs are strongly correlated with the matrix material and the type of metal inclusions (Figure 5). In terms of matrix, the DLC seems to be unquestionably superior. We attribute this to the mechanism of nucleating CNTs from DLC around Ni and Fe, as revealed previously by XPS (Figure 2). The SiC matrix is the intermediate case; the fairly good performance of the SiC:Ni catalyst might be attributed to the potential of SiC itself to be used as a template for the formation of graphene layers[49] that may fold around the Ni particles. Finally, the AlN matrix is the most inferior of all because AlN is inert to C deposition

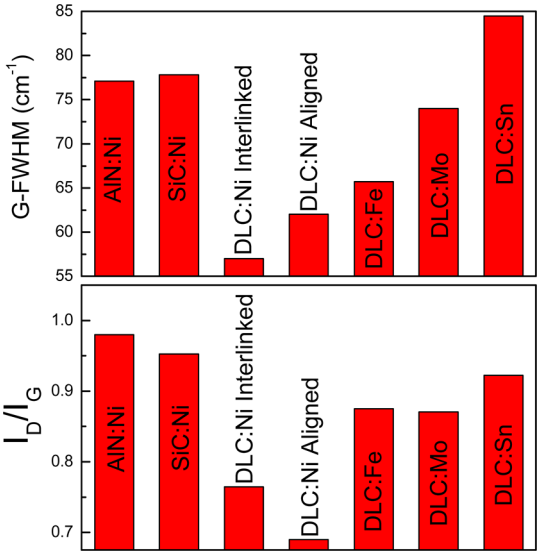

Figure 5. Basic Raman features of various nanocomposite catalyst templates using various combinations of matrix (DLC, SiC, AlN) and metal (Ni, Fe, Sn, Mo) materials.

and nucleation; hence, the only effect of AlN is to inhibit the growth of Ni and reduce the Ni particle size. In terms of metals, Ni and Fe performed better than Mo and Sn, in accordance to what is known for continuous metal films. However, the DLC:Ni and DLC:Fe catalyst templates are producing CNTs of higher quality than continuous Ni or Fe films due to their morphology that exhibits nanometer-wide features. According to Chen *et al.*,[50] small Ni crystals lower the driving force for the carbon diffusion through the Ni crystals, leading to low

final carbon yield; the low yield, however, is beneficial for the structural quality since the slower deposition provides the required time for growth close to equilibrium conditions, resulting in the elimination of structural defects.

More insights on the effect of the Ni grain size in the catalyst layer can be drawn by Scherrer's analysis of the grazing incidence X-ray diffraction (GIXRD) data (Figure 6a). In particular, CNTs grown using DLC:Ni catalyst, with fine Ni grain size (hardly identifiable by XRD), exhibit substantially lower I_D/I_G ratios compared to the CNTs grown using pure Ni catalyst layers deposited by PLD and sputtering (Figure 6b). Figure 6c,d shows the variations of the I_D/I_G ratio and of the broadening (full width at half maximum, fwhm) of the G peak *versus* the [Ni] content of the corresponding DLC:Ni catalyst. The I_D/I_G ratio was exceptionally low for all CNT systems grown on the DLC:Ni catalysts templates (Figure 6c) and decreased with [Ni]. The observed I_D/I_G and G-fwhm values are similar or lower than those reported for the best quality multiwalled CNTs so far,[13−15,47] indicating that the DLC:Ni catalyst improves substantially the structural quality of the grown CNTs. The G-fwhm increases with increasing [Ni] content in the DLC:Ni catalyst (Figure 3d), despite the subsequent decrease of I_D/I_G ratio. This is another indication of the gradual alignment of the CNTs with increasing [Ni] content in the catalyst layer since aligned multiwalled CNTs exhibit additional contributions to the G peak at 1575, 1590, and 1623 cm^{-1} due to additional vibration modes.[51] This is in accordance with the SEM images of Figure 1b.

Functional Properties of CNTs and Solar Applications. CNTs are inherently black (*i.e.*, they absorb all wavelengths of the visible light),[1,52−54] and in particular, low-density bundles of CNTs have been recently identified as perfect optical absorbers,[1] finding applications in stray light control[52] and cryptography,[53] and they have been proposed for applications in pyroelectric detectors and solar energy conversion.[1] In order to achieve ultra-blackness, a low refractive index and subsequently low density of CNTs is required,[54] as well as very high structural quality, in order to minimize light reflection by defects. The star-shaped CNTs produced on DLC:Ni meet these criteria.

After the in-depth morphological and structural characterization of the produced CNT systems of this work, the optical properties of the best of the produced CNTs (*i.e.*, those grown on DLC:Ni) have been thoroughly investigated. The produced CNTs exhibit exceptionally low optical reflection (acquired in the 240−790 nm range and in vertical incidence geometry); the reflectivity of the CNT samples for the three primary colors (red-green-blue) are displayed in Table 2. The reflectivity values for the fully dense sample D are similar to those of graphite.[1] On the contrary, the lowest density sample A exhibits reflectivity lower than 5×10^{-4}

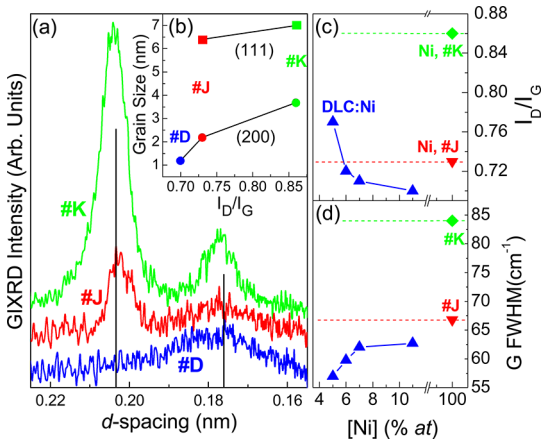

Figure 6. (a) GIXRD data of the various catalyst layers; the black bars indicate the reference diffraction lines of Ag powder. (b) Correlation of the Ni grain size with the I_D/I_G ratio of the CNTs. (c,d) I_D/I_G ratio and the G-fwhm of CNTs *vs* the Ni content on the catalyst, respectively.

for all wavelengths and, especially, less than 5×10^{-5} for the shorter wavelengths. In addition to the spectral dependence of optical reflectivity, the angular dependence of specular reflectivity of s- and p-polarized red light (657.5 nm) is also investigated; the relevant data for the marginal cases of samples A and D are presented in Figure 7a. The values for sample A are exceptionally low, at least 2 orders of magnitude less than those for sample D, which imply a very low refractive index as predicted by Garcia-Vidal *et al.*[54] and demonstrated by Yang *et al.*[1] and Shi *et al.*[53] It is worth noting that sample A consists of interlinked CNTs, suggesting that the alignment is not a prerequisite for producing super-black CNT-based materials; instead, the low density of the CNT samples seems to be the relevant essential feature.

The study of the surface scattering of light to nonspecular directions is essential since the produced CNTs, especially the low-density interlinked sample A, have very complex surfaces, exhibiting features of two length scales, that is, ~30 nm tube diameter and ~1 μm CNT bundle width. The off specular reflectivity has been measured by measuring the intensity of a 657.5 nm s-polarized laser beam while scanning the off specular angle ω around the specular angle of $\theta = 60°$ as presented in the inset of Figure 7a. The reflectivity values around the specular position $\theta = 30°$ ($\omega = 0°$) for the marginal cases of CNT samples A (low-density, interlinked) and D (fully dense, aligned), as well as for a gold mirror for comparison, are presented in Figure 7b. Both CNT samples exhibit a clear specular peak at $\omega = 0°$. This is quite different than what has been observed by Yang *et al.*[1] in low-density aligned tubes, most likely due to the higher density of our samples and the complex morphology of our CNTs. Nonetheless, even the specular reflection from sample A is exceptionally low, and the diffuse surface light scattering ($\omega \neq 0°$) is 2 orders of magnitude lower

TABLE 2. Main Properties of the CNTs Grown Using the DLC:Ni Templates

							reflectivity		
sample	morphology	density (g/cm^3)	resistance (kΩ)	I_D/I_G	G-fwhm (cm^{-1})	water contact angle (deg)	red 635 nm	green 535 nm	blue 475 nm
A	interlinked	1.8	27.438	0.77	57.0	165	5×10^{-4}	2×10^{-4}	$<5 \times 10^{-5}$
B	interlinked	2.1	10.099	0.72	59.8	112	4×10^{-3}	2×10^{-3}	1.4×10^{-3}
C	partially interlinked	2.14	1.745	0.71	62.1	105	2×10^{-2}	1.8×10^{-2}	1.5×10^{-2}
D	aligned	2.2	110.736	0.70	62.7	93	1.8×10^{-1}	1.4×10^{-1}	1.2×10^{-1}

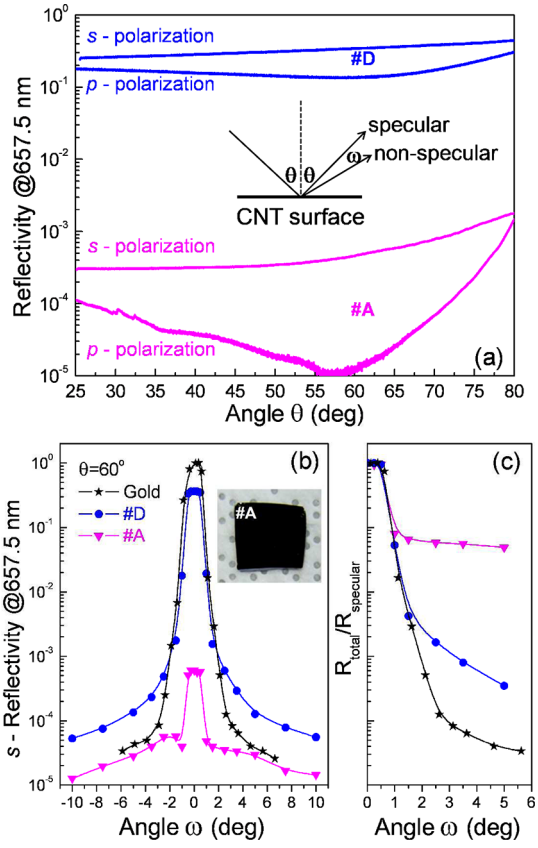

Figure 7. (a) Angular dependence of the specular reflectivity of s- and p-polarized red light for the marginal cases of samples A (low-density, interlinked CNTs) and D (fully dense aligned CNTs). (b) Off specular optical reflectivity at 657.5 nm of the same CNT samples; the inset shows the actual black appearance of sample A (photographed on standard clean room paper). (c) Ratio of the total reflectivity (specular and off specular) over the off specular component. The angles θ and ω are defined in the inset of (a).

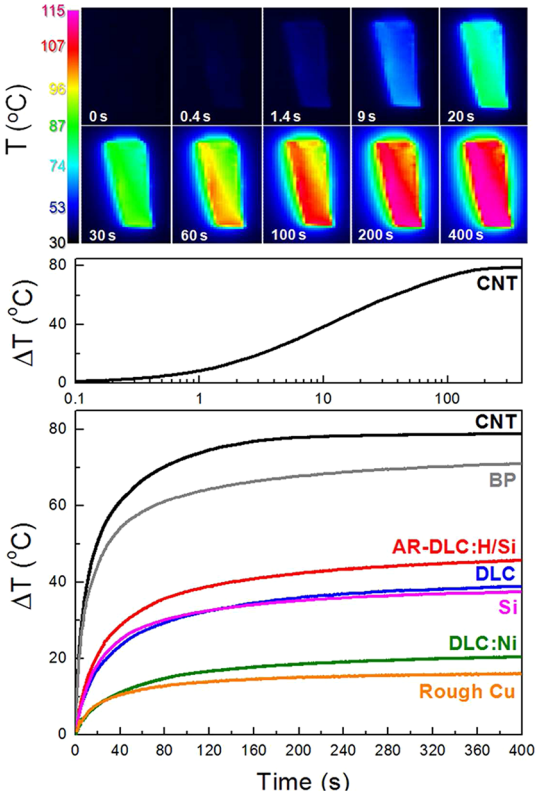

Figure 8. Bottom: Temperature's increase on the surface of the CNT sample A, due to exposure to the concentrated solar light in comparison to various reference samples such as (i) a bare Si wafer, (ii) commercial, rough, black paint (BP), (iii) a Si wafer coated by a hydrogenated DLC anti-reflection layer (AR-DLC:H/Si), (iv) the corresponding DLC:Ni catalyst layer, (v) a pure DLC film of intermediate sp^3 content (~50%), and (vi) a roughened Cu plate. Middle: Initial stages of temperature increase due to solar absorption by CNTs. Top: Snapshots from the thermal camera demonstrating the effective solar absorption by sample A, which is clearly resolved after 1 s exposure to sunlight.

(<10^{-5}). The diffuse surface light scattering for both samples A and D is substantially higher than that of the gold mirror (this is better illustrated in Figure 7c), proving that their overall optical response is greatly affected by their surface roughness.

Summarizing, the CNTs produced by this technology, especially the low-density interlinked CNTs similar to sample A, combine exceptional assets such as high optical absorption and low reflectivity over the whole visible spectrum, durability to environmental challenges, super-hydrophobic and, thus, self-cleaned surfaces, and high electrical and thermal conductivity.[6]

These assets make these materials promising for thermal harvesting of solar energy, such as in trough or parabolic collectors and solar water heaters. In order to investigate this perspective, we have set up the following solar simulation experiment. The divergent light of a solar simulator lamp is collected by a large-scale Fresnel lens and concentrated by a secondary lens to achieve a power density of 20 kW/m^2, which is a very moderate concentrated solar power, on the sample surface (refer also to Supporting Information). The sample temperature is monitored by a thermocouple

attached on the backside of the sample and by a mid-infrared thermal camera in front of the sample's surface. The CNT sample A is illuminated by the 20 kW/m^2 concentrated solar light, and its temperature *versus* time is recorded by the thermocouple and the thermal camera; the thermocouple and camera indications are in excellent agreement (in the range of ± 2 °C) for the CNT samples due to the high thermal conductivity of CNTs. The temperature increase of the CNT surface *versus* time, as recorded by the thermal camera in the middle of the sample, is shown in the bottom side of Figure 8 (black line); the spatial distribution of temperature on the CNT surface of sample A at various solar illumination times is demonstrated in the snapshots of the thermal camera in the top part of Figure 8, where the CNT sample A is clearly resolved from the background. In the middle part of Figure 8, the temporal evolution is presented in log-scale in order to reveal the dynamics of temperature increase on the CNT surface at the very initial stages of solar illumination. In addition to the CNT sample A, the corresponding thermal emission curves for a variety of reference samples include (i) commercial black acrylic matte paint (BP, gray line), (ii) the DLC:Ni catalysts film used for CNT growth (sample A, green line), (iii) a pure Si wafer surface (magenta line), (iv) a Si wafer coated by a hydrogenated DLC anti-reflection coating at 633 nm, grown by plasma-enhanced chemical vapor deposition (red line), and (v) an intentionally roughened Cu plate, which is the standard material of trough collectors (orange line), is also shown in the bottom part of Figure 8. It is evident that the super-black CNTs can achieve by far the highest temperature increase among all samples, demonstrating their substantial solar potential. The process might be more cost/energy-efficient and meet the industrial standards if the DLC:Ni templates are used in a low-temperature plasma CVD growth process of CNTs.[55,56]

CONCLUSIONS

Nanocomposite catalyst layers consisting of DLC matrices and various metal (Ni, Fe, Mo, Sn) nanoparticle inclusions have been produced by PLD; alternative matrices such as SiC and AlN have also been considered for comparison. The control of the metal particles at the nanoscale has been proven to be an efficient pathway for the development of durable and firmly attached CNTs of varying morphology (from interlinked star-shaped to aligned CNTs), tube thickness (30−100 nm), density, and structural quality. In particular, the low-density interlinked CNTs grown using the DLC:Ni templates exhibit an extraordinary combination of functional properties, such as super-hydrophobic surfaces, extreme optical absorption in the entirety of the visible range, exceptionally low optical reflection, and high thermal conductivity. This combination of assets of the produced CNTs offers a great potential for solar thermal applications that has been confirmed by the specially designed solar testing experiments performed in this work.

METHODS

Growth of Nanocomposite Catalysts. The samples were deposited on commercial Czochralski-grown, n-type Si(001) wafers in two steps: (i) PLD of the nanocomposite catalysts, and (ii) CVD of CNTs. The PLD system is equipped with a rotating target and sample holder. The rotating target consisted of pure, hot-pressed graphite or SiC or AlN and metal (Ni, Fe, Mo, Sn) plates having the form of two opposing sectors. The distance between the target and the substrate was 30 mm. The thickness of the films ranged between 23 and 35 nm. The hard-focused laser beam was the third harmonic (λ = 355 nm) of a Nd:YAG laser (Lambda-Physik, 6 ns pulse duration, 10 Hz repetition rate, and 35 mJ pulse energy). Pure Ni films were deposited by PLD (using a pure Ni target) as well as by magnetron sputtering for comparison purposes.

Growth of CNTs. For the synthesis of CNTs, the nanocomposite catalyst layers were placed in an alumina crucible within a quartz tube, located in a horizontal tubular furnace. The samples were heated to the desired temperature (700 °C) under argon atmosphere. The carbon precursor [acetylene (99.6% pure)] and the carrier gas (Ar, 99.999% pure) were introduced into the reactor at flow rates of 10 and 90 sccm, respectively, when the temperature was stabilized to 700 °C. The reaction took place for 15 or 30 min; after the completion of the reaction, the ceramic boat was cooled to room temperature under argon atmosphere.

Microscopy. Optical microscopy observations of the produced CNTs have been acquired in an Olympus metallographic microscope using white fluorescent lamp illumination. Scanning electron microscopy images were recorded in a JEOL JSM-5260 scanning electron microscope with a W filament. Chemical microanalysis has been carried out in the SEM by energy-dispersive X-ray spectroscopy using an Oxford Instruments X-ray analyzer. For the study of the DLC:Ni surfaces, atomic force microscopy images were obtained in tapping mode with a Bruker Multimode Nanoscope 3D using RTESP n-type silicon cantilevers.

Chemical Analysis. The *in situ* electron-excited Auger electron spectra of the catalyst layers were acquired using a 1 keV (for sp^3 determination) and 3 keV (for the determination of [Ni]/[C]) primary electron beam from a thermionic W electron gun, which is located concentrically into a cylindrical mirror analyzer by Physical Electronics. The *ex situ* X-ray photoelectron spectra and X-ray-excited Auger electron spectra were acquired in a surface analysis ultrahigh vacuum system (SPECS GmbH) equipped with a twin Al−Mg anode X-ray source and a multichannel hemispherical sector electron analyzer (HSA-Phoibos 100). The pass energy was 20 eV, providing a fwhm of 1.18 eV for the Ag 3d line. XPS spectra have been acquired after *in situ* annealing at the temperature of T-CVD growth of CNTs (700 °C) inside the ultrahigh vacuum system.

X-ray Methods. Grazing incidence X-ray diffraction, specular X-ray reflectivity, and off specular diffuse reflectivity/scattering data were acquired in a Bruker D8-Avance diffractometer equipped with a Göbel mirror, parallel beam optics, a reflectivity sample stage with a knife edge, and a linear stripe detector (LynxEye), using the Cu Kα line.

Optical and Electrical Characterization. Raman spectra were recorded with a micro-Raman system (RM1000 Renishaw) using a

laser excitation line at 532 nm (Nd:YAG) in the range of 100−3500 cm^{-1}. A 0.5−1 mW power was used with 1 μm focus spot in order to avoid photodecomposition of the samples. Optical reflectivity spectra were acquired in the 240−790 nm range at near-normal incidence using a white light deuterium−halogen source, a coaxial fiber-optic assembly, a high line density grating, and a CCD detector (Avantes); the reflectivity spectra were normalized using two reference mirrors of sputtered silver and gold. Variable-angle optical reflectivity (specular and off specular) measurements were carried out in an in-house-built instrument consisting of a solid-state laser source (657.5 nm), an analog photometer, and a high accuracy goniometer capable of independent movement of the θ and 2θ circles; the values were normalized using the specular reflection of gold and silver mirrors. The DC electrical resistance values of the produced CNTs have been determined from $I-V$ measurements acquired in a four-probe station, using a Keithley 2410 high-voltage source meter.

Solar Testing. The solar absorption from CNTs has been recorded by an infrared camera (CEDIP MWIR) with a cooled InSb detector (waveband 3−5 μm), a frame rate of 150 Hz, and resolution of 25 mK and using an integration time of 345 μs. The solar simulator setup is consisted of the following: (A) a solar emission lamp (Sciencetech SF150, 150 W), (B) a UV (<400 nm) filter, (C) acrylic Fresnel focusing lens (Edmund Optics), (D) a quartz, plane convex, near-field, focusing lens, (E) sample, resulting in a solar power of 20 W/cm^2 measured by a MELLES-GRIOT broad-band power and energy meter system (PEM-2 W).

Conflict of Interest: The authors declare no competing financial interest.

Acknowledgment. The authors are acknowledging the Network of Central Facilities of the University of Ioannina for using their infrastructure, in particular, the Department of Physics and the Central Laser Facility (XPS and PLD, respectively), the Central Microscopy Lab (SEM), and the Nanotechnology Lab (four-probe measurements and solar simulator). Part of this work has been performed during the sabbatical visit of P.P. at the Cyprus University of Technology. L.K. acknowledges financial support by the Research Promotion Foundation of the Republic of Cyprus and the European Regional Fund (ERF) Grant DESMI 2008 - Strategic Infrastructure "Research Unit for Nanostructured Materials Systems". E.D. acknowledges financial support by the European Union—European Social Fund (ESF) and National Sources, in the framework of the program "HERAKLEITOS II" of the "Operational Program Education and Life Long Learning" of the Hellenic Ministry of Education, Life-Long Learning, and Religious Affairs.

Supporting Information Available: Material growth and processing; additional microscopy images; additional chemical analysis; details of X-ray methods; optical and electrical characterization; details of solar testing. This material is available free of charge *via* the Internet at http://pubs.acs.org.

REFERENCES AND NOTES

1. Yang, Z.-P.; Ci, L.; Bur, J. A.; Lin, S.-Y.; Ajayan, P. M. Experimental Observation of an Extremely Dark Material Made by a Low-Density Nanotube Array. *Nano Lett.* **2008**, *8*, 446–451.
2. Kymakis, E.; Amaratunga, G. A. J. Single-Wall Carbon Nanotube/Conjugated Polymer Photovoltaic Devices. *Appl. Phys. Lett.* **2002**, *80*, 112–114.
3. Guldi, D. M.; Rahman, G. M. A.; Zerbetto, F.; Prato, M. Carbon Nanotubes in Electron Donor−Acceptor Nanocomposites. *Acc. Chem. Res.* **2005**, *38*, 871–878.
4. Avouris, P.; Freitag, M.; Perebeinos, V. Carbon-Nanotube Photonics and Optoelectronics. *Nat. Photonics* **2008**, *2*, 341–350.
5. Hasan, T.; Sun, Z.; Wang, F.; Bonaccorso, F.; Tan, P. H.; Rozhin, A. G.; Ferrari, A. C. Nanotube−Polymer Composites for Ultrafast Photonics. *Adv. Mater.* **2009**, *21*, 3874–3899.
6. Mingo, N.; Broido, D. A. Length Dependence of Carbon Nanotube Thermal Conductivity and the Problem of Long Waves. *Nano Lett.* **2005**, *5*, 1221–1225.
7. Huang, H.; Liu, C.; Wu, Y.; Fan, S. Aligned Carbon Nanotube Composite Films for Thermal Management. *Adv. Mater.* **2005**, *17*, 1652–1656.
8. Zhong, G.; Hofmann, S.; Yan, F.; Telg, H.; Warner, J. H.; Eder, D.; Thomsen, C.; Milne, W. I.; Robertson, J. Acetylene: A Key Growth Precursor for Single-Walled Carbon Nanotube Forests. *J. Phys. Chem. C* **2009**, *113*, 17321–17325.
9. Jackson, J. J.; Puretzky, A. A.; More, K. L.; Rouleau, C. M.; Eres, G.; Geohegan, D. B. Pulsed Growth of Vertically Aligned Nanotube Arrays with Variable Density. *ACS Nano* **2010**, *4*, 7573–7581.
10. In, J. B.; Grigoropoulos, C. P.; Chernov, A. A.; Noy, A. Hidden Role of Trace Gas Impurities in Chemical Vapor Deposition Growth of Vertically-Aligned Carbon Nanotube Arrays. *Appl. Phys. Lett.* **2011**, *98*, 153102.
11. Yudasaka, M.; Kasuya, Y.; Kokai, F.; Takahashi, K.; Takizawa, M.; Bandow, S.; Iijima, S. Causes of Different Catalytic Activities of Metals in Formation of Single-Wall Carbon Nanotubes. *Appl. Phys.* **2002**, *A74*, 377–385.
12. Rümmeli, M. H.; Borowiak-Palen, E.; Gemming, T.; Pichler, T.; Knupfer, M.; Kalbác, M.; Dunsch, L.; Jost, O.; Silva, S. R. P.; Pompe, W.; *et al.* Novel Catalysts, Room Temperature, and the Importance of Oxygen for the Synthesis of Single-Walled Carbon Nanotubes. *Nano Lett.* **2005**, *5*, 1209–1215.
13. Tsoufis, T.; Xidas, P.; Jankovic, L.; Gournis, D.; Saranti, A.; Bakas, T.; Karakassides, M. A. Catalytic Production of Carbon Nanotubes over Fe−Ni Bimetallic Catalysts Supported on MgO. *Diamond Relat. Mater.* **2007**, *16*, 155–160.
14. Zhao, B.; Futaba, D. N.; Yasuda, S.; Akoshima, M.; Yamada, T.; Hata, K. Exploring Advantages of Diverse Carbon Nanotube Forests with Tailored Structures Synthesized by Supergrowth from Engineered Catalysts. *ACS Nano* **2009**, *3*, 108–114.
15. Cantoro, M.; Hofmann, S.; Mattevi, C.; Pisana, S.; Parvez, A.; Fasoli, A.; Ducati, C.; Scardaci, V.; Ferrari, A. C.; Robertson, J. Plasma Restructuring of Catalysts for Chemical Vapor Deposition of Carbon Nanotubes. *J. Appl. Phys.* **2009**, *105*, 064304.
16. Li, Y.; Cui, R.; Ding, L.; Liu, Y.; Zhou, W.; Zhang, Y.; Jin, Z.; Peng, F.; Liu, J. How Catalysts Affect the Growth of Single-Walled Carbon Nanotubes on Substrates. *Adv. Mater.* **2010**, *22*, 1508–1515.
17. Musso, S.; Porro, S.; Giorcelli, M.; Chiodoni, A.; Ricciardi, C.; Tagliaferro, A. Macroscopic Growth of Carbon Nanotube Mats and Their Mechanical Properties. *Carbon* **2007**, *45*, 1133–1136.
18. Steiner, S. A.; Baumann, T. F.; Bayer, B. C.; Blume, R.; Worsley, M. A.; Moberly-Chan, W. J.; Shaw, E. L.; Schlögl, R.; Hart, A. J.; Hofmann, S.; *et al.* Nanoscale Zirconia as a Nonmetallic Catalyst for Graphitization of Carbon and Growth of Single- and Multiwall Carbon Nanotubes. *J. Am. Chem. Soc.* **2009**, *131*, 12144–12154.
19. Orbaek, A. W.; Owens, A. C.; Barron, A. R. Increasing the Efficiency of Single Walled Carbon Nanotube Amplification by Fe-Co Catalysts through the Optimization of CH_4/H_2 Partial Pressures. *Nano Lett.* **2011**, *11*, 2871–2874.
20. Saenger, K. L.; Tsang, J. C.; Bol, A. A.; Chu, J. O.; Grill, A.; Lavoie, C. *In Situ* X-ray Diffraction Study of Graphitic Carbon Formed during Heating and Cooling of Amorphous-C/Ni Bilayers. *Appl. Phys. Lett.* **2010**, *96*, 153105.
21. Matenoglou, G.; Evangelakis, G. A.; Kosmidis, C.; Foulias, S.; Papadimitriou, D.; Patsalas, P. Pulsed Laser Deposition of Amorphous Carbon/Silver Nanocomposites. *Appl. Surf. Sci.* **2007**, *253*, 8155–8159.
22. Siozios, A.; Koutsogeorgis, D. C.; Lidorikis, E.; Dimitrakopoulos, G. P.; Kehagias, Th.; Zoubos, H.; Komninou, Ph.; Cranton, W. M.; Kosmidis, C.; Patsalas, P. Optical Encoding by Plasmon-Based Patterning: Hard and Inorganic Materials Become Photosensitive. *Nano Lett.* **2012**, *12*, 259–263.
23. Kassavetis, S.; Patsalas, P.; Logothetidis, S.; Robertson, J.; Kennou, S. Dispersion Relations and Optical Properties of Amorphous Carbons. *Diamond Relat. Mater.* **2007**, *16*, 1813–1822.
24. Quintana, M.; Spyrou, K.; Grzelczak, M.; Browne, W. R.; Rudolf, P.; Prato, M. Functionalization of Graphene *via* 1,3-Dipolar Cycloaddition. *ACS Nano* **2010**, *4*, 3527–3533.

25. Patsalas, P.; Logothetidis, S.; Kelires, P. C. Surface and Interface Morphology and Structure of Amorphous Carbon Thin and Multilayer Films. *Diamond Relat. Mater.* **2005**, *14*, 1241–1254.
26. Pham-Huua, C.; Vieira, R; Louis, B.; Carvalho, A.; Amadou, J.; Dintzer, T.; Ledoux, M. J. About the Octopus-like Growth Mechanism of Carbon Nanofibers over Graphite Supported Nickel Catalyst. *J. Catal.* **2006**, *240*, 194–202.
27. Saavedra, M. S.; Sims, G. D.; McCartney, L. N.; Stolojan, V.; Anguita, J. V.; Tan, Y. Y.; Ogin, S. L.; Smith, P. A.; Silva, S. R. P. Catalysing the Production of Multiple Arm Carbon Octopi Nanostructures. *Carbon* **2012**, *50*, 2141–2146.
28. El Mel, A. A.; Achour, A.; Xu, W.; Choi, C. H.; Gautron, E.; Angleraud, B.; Granier, A.; Le Brizoual, L.; Djouadi, M. A.; Tessier, P. Y. Hierarchical Carbon Nanostructure Design: Ultra-Long Carbon Nanofibers Decorated with Carbon Nanotubes. *Nanotechnology* **2011**, *22*, 435302.
29. Robertson, J. Diamond-like Amorphous Carbon. *Mater. Sci. Eng., R* **2002**, *37*, 129–281.
30. Ferrari, A. C.; Libassi, A.; Tanner, B. K.; Stolojan, V.; Yuan, J.; Brown, L. M.; Rodil, S. E.; Kleinsorge, B.; Robertson, J. Density, sp^3 Fraction, and Cross-Sectional Structure of Amorphous Carbon Films Determined by X-ray Reflectivity and Electron Energy-Loss Spectroscopy. *Phys. Rev.* **2000**, *B62*, 11089–11103.
31. McIntyre, N. S.; Cook, M. G. X-ray Photoelectron Studies on Some Oxides and Hydroxides of Cobalt, Nickel, and Copper. *Anal. Chem.* **1975**, *47*, 2208–2213.
32. Sygellou, L.; Ladas, S. Interfacial Effects in Ultra-Thin Nickel Deposits on Yttria-Stabilized Zirconia. *Surf. Sci.* **2004**, *566–568*, 698–702.
33. Patsalas, P.; Handrea, M.; Logothetidis, S.; Gioti, M.; Kennou, S.; Kautek, W. A Complementary Study of Bonding and Electronic Structure of Amorphous Carbon Films by Electron Spectroscopy and Optical Techniques. *Diamond Relat. Mater.* **2001**, *10*, 960–964.
34. Calliari, L. AES and Core Level Photoemission in the Study of a-C and a-C:H. *Diamond Relat. Mater.* **2005**, *14*, 1232–1240.
35. Kovács, G. J.; Bertóti, I.; Radnóczi, G. X-ray Photoelectron Spectroscopic Study of Magnetron Sputtered Carbon–Nickel Composite Films. *Thin Solid Films* **2008**, *516*, 7942–7946.
36. Cao, Y.; Nyborg, L.; Jelvestam, U. XPS Calibration Study of Thin-Film Nickel Silicides. *Surf. Interface Anal.* **2009**, *41*, 471–483.
37. Amara, H.; Roussel, J.-M.; Bichara, C.; Gaspard, J.-P.; Ducastelle, F. Tight-Binding Potential for Atomistic Simulations of Carbon Interacting with Transition Metals: Application to the Ni-C System. *Phys. Rev.* **2009**, *B79*, 014100.
38. Jacobson, P.; Stöger, B.; Garhofer, A.; Parkinson, G. S.; Schmid, M.; Caudillo, R.; Mittendorfer, F.; Redinger, J.; Diebold, U. Nickel Carbide as a Source of Grain Rotation in Epitaxial Graphene. *ACS Nano* **2012**, *6*, 3564–3572.
39. Hofmann, S.; Sharma, R.; Ducati, C.; Du, G.; Mattevi, C.; Cepek, C.; Cantoro, M.; Pisana, S.; Parvez, A.; Cervantes-Sodi, F.; *et al. In Situ* Observations of Catalyst Dynamics during Surface-Bound Carbon Nanotube Nucleation. *Nano Lett.* **2007**, *7*, 602–608.
40. Yoshida, H.; Takeda, S.; Uchiyama, T.; Kohno, H.; Homma, Y. Atomic-Scale *In Situ* Observation of Carbon Nanotube Growth from Solid State Iron Carbide Nanoparticles. *Nano Lett.* **2008**, *8*, 2082–2086.
41. Page, A. J.; Yamane, H.; Ohta, Y.; Irle, S.; Morokuma, K. QM/MD Simulation of SWNT Nucleation on Transition-Metal Carbide Nanoparticle. *J. Am. Chem. Soc.* **2010**, *132*, 15699–15707.
42. Börjesson, A.; Bolton, K. First Principles Studies of the Effect of Nickel Carbide Catalyst Composition on Carbon Nanotube Growth. *J. Phys. Chem. C* **2010**, *114*, 18045–18050.
43. Benito, S. P.; Lefferts, L. Influence of Reaction Parameters on the Attachment of a Carbon Nanofiber Layer on Ni Foils. *Surf. Coat. Technol.* **2012**, *206*, 3366–3373.
44. Sinha, S. K.; Sirota, E. B.; Garoff, S.; Stanley, H. B. X-ray and Neutron Scattering from Rough Surfaces. *Phys. Rev. B* **1988**, *38*, 2297–2311.
45. Brennan, T.; Hughes, A. V.; Roser, S. J.; Mann, S.; Edler, K. J. Concentration-Dependent Formation Mechanisms in Mesophase Silica-Surfactant Films. *Langmuir* **2002**, *18*, 9838–9844.
46. Purewal, M. S.; Hong, B. H.; Ravi, A.; Chandra, B.; Hone, J.; Kim, P. Scaling of Resistance and Electron Mean Free Path of Single-Walled Carbon Nanotubes. *Phys. Rev. Lett.* **2007**, *98*, 186808.
47. Chhowalla, M.; Teo, K. B. K.; Ducati, C.; Rupesinghe, N. L.; Amaratunga, G. A. J.; Ferrari, A. C.; Roy, D.; Robertson, J.; Milne, W. I. Growth Process Conditions of Vertically Aligned Carbon Nanotubes Using Plasma Enhanced Chemical Vapor Deposition. *J. Appl. Phys.* **2001**, *90*, 5308–5317.
48. Saito, R.; Hofmann, M.; Dresselhaus, G.; Jorio, A.; Dresselhaus, M. S. Raman Spectroscopy of Graphene and Carbon Nanotubes. *Adv. Phys.* **2011**, *60*, 413–550.
49. Strupinski, W.; Grodecki, K.; Wysmolek, A.; Stepniewski, R.; Szkopek, T.; Gaskell, P. E.; Grüneis, A.; Haberer, D.; Bozek, R.; Krupka, J.; *et al.* Graphene Epitaxy by Chemical Vapor Deposition on SiC. *Nano Lett.* **2011**, *11*, 1786–1791.
50. Chen, D.; Christensen, K. O.; Ochoa-Fernández, E.; Yu, Z.; Tøtdal, B.; Latorre, N.; Monzón, A.; Holmen, A. Synthesis of Carbon Nanofibers: Effects of Ni Crystal Size during Methane Decomposition. *J. Catal.* **2005**, *229*, 82–96.
51. Rao, A. M.; Jorio, A.; Pimenta, M. A.; Dantas, M. S. S.; Saito, R.; Dresselhaus, G.; Dresselhaus, M. S. Polarized Raman Study of Aligned Multiwalled Carbon Nanotubes. *Phys. Rev. Lett.* **2000**, *84*, 1820–1823.
52. Butler, J. J.; Georgiev, G. T.; Tveekrem, J. L.; Quijada, M.; Getty, S.; Hagopian, J. G. Initial Studies of the Bidirectional Reflectance Distribution Function of Carbon Nanotube Structures for Stray Light Control Applications. *Proc. SPIE* **2010**, 78620D.
53. Shi, H.; Ok, J. G.; Baac, H. W.; Guo, L. J. Low Density Carbon Nanotube Forest as an Index-Matched and near Perfect Absorption Coating. *Appl. Phys. Lett.* **2011**, *99*, 211103.
54. Garcia-Vidal, F. J.; Pitarke, J. M.; Pendry, J. B. Effective Medium Theory of the Optical Properties of Aligned Carbon Nanotubes. *Phys. Rev. Lett.* **1997**, *78*, 4289–4292.
55. Shang, N. G.; Tan, Y. Y.; Stolojan, V; Papakonstantinou, P.; Silva, S. R. P. High-Rate Low-Temperature Growth of Vertically Aligned Carbon Nanotubes. *Nanotechnology* **2010**, *21*, 505604.
56. Cantoro, M .; Hofmann, S.; Pisana, S.; Scardaci, V.; Parvez, A.; Ducati, C.; Ferrari, A. C.; Blackburn, A. M.; Wang, K.-Y.; Robertson, J. Catalytic Chemical Vapor Deposition of Single-Wall Carbon Nanotubes at Low Temperatures. *Nano Lett.* **2006**, *6*, 1107–1112.